Lattice models for ballistic aggregation: Cluster-shape-dependent exponents

Fahad Puthalath [1,2,*] Apurba Biswas [3,4,†] V. V. Prasad,[5,‡] and R. Rajesh[3,4,§]

[1]*Institut für Materialphysik im Weltraum, Deutsches Zentrum für Luft- und Raumfahrt (DLR), 51170 Köln, Germany*

[2]*Institut für Theoretische Physik, Universität zu Köln, Zülpicher Strasse 77, 50937 Köln, Germany*

[3]*The Institute of Mathematical Sciences, C.I.T. Campus, Taramani, Chennai 600113, India*

[4]*Homi Bhabha National Institute, Training School Complex, Anushakti Nagar, Mumbai 400094, India*

[5]*Department of Physics, Cochin University of Science and Technology, Cochin 682022, India*

We study ballistic aggregation on a two-dimensional square lattice, where particles move ballistically in between momentum and mass conserving coalescing collisions. Three models are studied based on the shapes of the aggregates: In the first the aggregates remain point particles, in the second they retain the fractal shape at the time of collision, and in the third they assume a spherical shape. The exponents describing the power-law temporal decay of number of particles and energy as well as dependence of velocity correlations on mass are determined using large-scale Monte Carlo simulations. It is shown that the exponents are universal only for the point-particle model. In the other two cases, the exponents are dependent on the initial number density and correlations vanish at high number densities. The fractal dimension for the second model is close to 1.49.

I. INTRODUCTION

There is a wide variety of physical phenomena at different length scales in which aggregation of particles and clusters to form larger particles is the predominant dynamical process [1]. Examples include aerosols [2,3], agglomeration of soot [4,5], gelation [6], cloud formation [7], colloidal agrregates [8], astrophysical problems [9], aggregation of dust particles in planetary discs [10–12], dynamics of Saturn's rings [11,13], polyelectrolytes [14,15], networks [16], etc. A minimal model that focuses only on the effects of aggregation is the cluster-cluster aggregation (CCA) model in which particles that come into contact undergo mass-conserving coalescence (reviews may be found in Refs. [17–19]). In addition to its relevance for different physical phenomena, CCA has also been studied as a nonequilibrium system undergoing scale-invariant dynamics that is described by exponents that depend only on very generic features of the transport process. This universal feature allows applications of results for CCA in seemingly unrelated systems like Burgers turbulence [20–24], Kolmogorov self-similar scaling [25–27], granular systems [28–31], hydrodynamics of run and tumble particles [32], evolution of planetesimals [33], geophysical flows [34], etc.

Among the different transport processes, ballistic transport is of particular importance and the resultant CCA is known as the ballistic aggregation (BA) model, the focus of this paper. In the BA model, momentum is additionally conserved in collisions. The BA model with spherical particles has been studied using mean-field theory, large-scale simulations in two and three dimensions, and is exactly solvable in one dimension. It is found that the number of particles, $n(t)$, and energy, $e(t)$, decrease with time, t, as power laws: $n(t) \propto t^{-\theta_n}$, $e(t) \propto t^{-\theta_e}$. These exponents have been determined in d dimensions within a mean-field approximation which assumes that the particle density is small, that the particles are compact spherical clusters of equal density, and that the velocities of the particles constituting a cluster are uncorrelated. Within these assumptions, scaling arguments predict the existence of a growing length scale $\mathcal{L}_t \sim t^{1/z^{\mathrm{mf}}}$ with $z^{\mathrm{mf}} = (d+2)/2d$ and mean-field exponents, $\theta_n^{\mathrm{mf}} = 2d/(d+2)$ and $\theta_e^{\mathrm{mf}} = \theta_n^{\mathrm{mf}}$ [35]. The correlations in the initial velocities of the constituents of a cluster is characterized by an exponent η: $\langle v_m^2 \rangle \sim m^{-\eta}$, where $\langle v_m^2 \rangle$ is the mean-square velocity of a particle of mass m. In the mean-field approximation, by assumption, $\eta^{\mathrm{mf}} = 1$. The mean-field results for the exponents are of particular significance to the study of the unrelated problem of freely cooling granular gas in which ballistic particles undergo energy-dissipating, momentum conserving binary collisions. It has been shown that an exponent characterizing the energy decay in the granular gas is equal to θ_e^{mf} in dimensions up to three [28,30,36].

In one dimension, BA is exactly solvable and the exponents match with the mean-field exponents [21,37–39]. However, in two and three dimensions, it has been shown that the exponents for BA with spherical particles depend on the initial number density n_0. In two dimensions and for dilute systems ($n_0 \to 0$), it has been shown that the numerically obtained θ_n is 17% larger than θ_n^{mf} because of strong velocity correlations between colliding aggregates, with η decreasing from $\eta \approx 1.33$ for low densities to $\eta \approx 1 = \eta^{\mathrm{mf}}$ for high densities [30,40–43]. In three dimensions, it is found that as n_0 increases from 0.005 to 0.208, θ_e decreases from $\theta_e = 1.283$ to 1.206 and appears to converge to the $\theta_e^{\mathrm{mf}} = 1.2$ with

*fahad.puthalath@dlr.de

†apurbab@imsc.res.in

‡prasadvv@cusat.ac.in

§rrajesh@imsc.res.in

increasing n_0, and η decreases from $\eta \approx 1.23$ for low densities to $\eta \approx 1 = \eta^{\mathrm{mf}}$ for high densities [30,43]. It is remarkable that the mean-field results describe well only the systems with large n_0, while its derivation assumes the limit $n_0 \to 0$. This counterintuitive result has been argued to be due to the randomization of the velocities at higher densities due to an avalanche of coagulation events that occur due to the overlap of a newly created spherical particle with already existing particles as the number density is increased.

While the kinetics of BA with spherical particles are reasonably understood, much less is known for the exponents when clusters have nonspherical shapes. The scaling analysis can be extended to the case when the mass scales with radius with a fractal dimension d_f [41] (also see Sec. III, where we review scaling theory). The scaling theory leads to hyperscaling relations between the different exponents independent of the mean-field assumptions. Fractal shapes are of particular importance in the case of the experiments on aggregates of soot [5,44], mammary epithelial cells [45,46], spray flames [47], etc., where the aggregates have a fractal dimension different from those of compact structures ($d_f = 2, 3$). While the fractal dimensions seen in experiments [5,45] are sometimes close to that for diffusion-limited aggregation (DLA) ($d_f \approx 1.7$), there are many examples for which it is very different (for instance, 1.54 for sprays [47], 1.5 for cells [46], or 2.4 for soot [44]). The fractal dimension of aggregates formed by ballistic motion is not known to the best of our knowledge. In addition, it is also not known how the exponents for BA change when the shape of the clusters deviates from spherical. Neither is it known whether the mean-field limit is reached for any particular limit of number density when the clusters are fractal. Finally, in the characterization of mass distribution, a relevant exponent is the scaling of mass distribution with small mass, namely, $N(m) \sim m^\zeta$ [also see definition in Eq. (6)]. The exponent ζ is an independent exponent and cannot be obtained from scaling theory, and is not known even for BA with spherical particles.

To answer these questions, we study three differently shaped clusters (named models A, B, C) undergoing BA on the square lattice. We choose a lattice approach as it allows us to maintain fractal shapes in a computationally efficient manner. Lattice models are known to reproduce the same results as the continuum for BA in one dimension [24,48], and we expect the equivalence to hold true for two and higher dimensions. In model A, the clusters occupy a single site irrespective of its mass. This limiting model allows us to separate the dependence of the velocity correlations on the initial density from the dependence on the mass-dependent shape. In model B, we study clusters where the clusters maintain the shape at the time of contact. Such clusters turn out to be fractal. In model C, we study spherical clusters in which the lattice approximation to the disk is maintained. This model allows us to study lattice effects by comparing the results on the lattice with the continuum results. In addition, we obtain the value of the exponent ζ for all three models. The results for the three models are summarized in Table II (model A), Table III and Fig. 17 (model B), Table IV and Fig. 23 (model C). For model A, we show that the exponents are universal, in the sense that it is independent of the initial number density, n_0, and it is

TABLE I. Simulation details.

Model	L's simulated	Number densities (n_0)
A	upto 1000	0.01–1.00
B	upto 10000	0.001–0.01
C	upto 10000	0.0001–0.16

different from the mean-field results. For models B and C, we find that the exponents are dependent on n_0 and approach the mean-field assumptions of uncorrelated velocities only in the limit of large n_0. The fractal dimension for model B, on the other hand, is universal, with $d_f \approx 1.49$.

The remainder of the paper is organized as follows. Section II contains a definition of the different models as well as a description of the simulation methods. We briefly review the scaling theory for BA with differently shaped particles in Sec. III. In Sec. IV, for the three models, we describe the results for the different exponents obtained from large-scale Monte Carlo simulations. Section V contains a summary and discussion of the results.

II. MODEL

In this section, we define the three models that we study in this paper. Consider a square lattice of size $L \times L$ with periodic boundary conditions. Initially, N particles, each of mass 1, are randomly distributed with a site having utmost one particle. Each particle is assigned a velocity whose magnitude is drawn from a uniform distribution in $[0,1)$ and whose direction is chosen uniformly in $[0, 2\pi)$. The velocity of the center of mass is set to be zero by choosing an appropriate frame of reference. The system evolves stochastically in time as follows. A particle with velocity (v_x, v_y) hops in the x direction with rate $|v_x|$ in the positive (negative) direction depending on whether v_x is positive (negative). Likewise, it hops along the y axis with rate $|v_y|$ in the direction determined by the sign of v_y. When two particles collide, they aggregate to form a new particle. The mass of the new particle is the sum of the constituent particles while the new velocity is determined by conservation of linear momentum. The shape of the new particle is determined based on three different rules, leading to three different models.

A. Model A: Point particles

In model A, when a particle hops onto a site which is already occupied, then the two particles coalesce, conserving

TABLE II. Summary of the numerically obtained values of the exponents for model A. The values are independent of initial density n_0.

Exponent	Value
θ_n	0.633(7)
θ_e	0.728(5)
η	1.1505(3)
ζ	0.270(5)

TABLE III. Summary of the numerically obtained values of the exponents for model B.

n_0	θ_n	η	θ_e $(=\eta\theta_n)$	d_f	d_f [Eq. (18)]	ζ
0.00100	1.01(5)	1.291(4)	1.30(7)	1.49(3)	1.54(17)	−0.41(5)
0.00125	1.01(8)	1.293(4)	1.30(10)	1.49(3)	1.54(23)	−0.42(1)
0.00250	1.03(4)	1.261(7)	1.30(6)	1.49(3)	1.52(14)	−0.46(2)
0.00500	1.08(4)	1.231(2)	1.33(5)	1.49(3)	1.46(12)	−0.49(2)
0.01	1.10(2)	1.204(3)	1.32(3)	1.49(3)	1.45(7)	−0.54(2)
0.04		1.10				
0.08		1.08				
0.16		1.05				

mass and momentum. The new particle occupies the same lattice site. We call this model the point-particle model, since the sizes of all the particles are the same (one lattice site) irrespective of their mass. The model is motivated from its similar counterpart in one dimension as considered in Ref. [24].

B. Model B: Fractal clusters

In model *B*, the particles, also referred to as clusters, are extended objects consisting of a collection of sites that are linked to each other by nearest-neighbor bonds. When a cluster hops, if any of the lattice sites belonging to it becomes adjacent to a site belonging to another cluster, then the two clusters coalesce. The new cluster maintains the shape at the time of coalescing, till it collides with another cluster at a future time. The new velocity of the cluster is determined through momentum conservation. Snapshots of the configuration at different times are shown in Fig. 1. The clusters are extended and will be shown to be fractals. Model B is motivated from the study of aggregation in two dimensions in the continuum model as considered in Ref. [49].

C. Model C: Spherical clusters

In model *C*, like in model *B*, particles are extended clusters. However, the shape of these particles is constrained to be spherical. When two particles come into contact, they are replaced by a new spherical particle. The center of mass of the new particle is chosen to be the lattice site closest to the center of mass of the constituent particles. To construct a spherical cluster on the square lattice, we fill all lattice sites within circles of increasing radius. The sites in the outermost shell, if not fully occupied, are chosen at random. This rearrangement of sites to form a spherical shape will, at times, lead to the new

TABLE IV. Summary of the numerically obtained values of the exponents for model C.

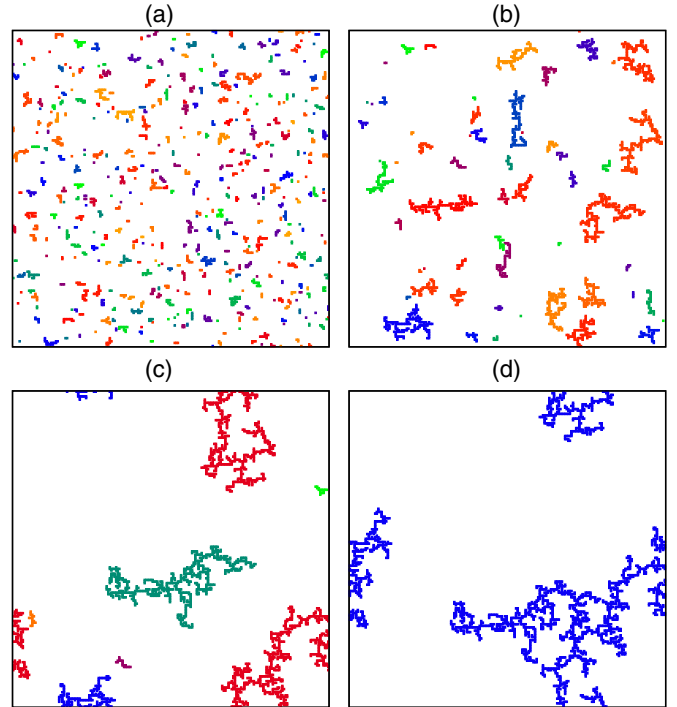| n_0	θ_n	η	$\theta_e(=\eta\theta_n)$	ζ
0.0001	0.83(4)	1.283(13)	1.06(6)	−0.248(26)
0.00125	0.84(5)	1.275(10)	1.07(7)	−0.350(27)
0.01	0.85(5)	1.241(2)	1.05(6)	−0.364(6)
0.04	0.87(6)	1.174(3)	1.02(7)	−0.403(4)
0.16	0.93(5)	1.114(2)	1.04(6)	−0.563(10)

FIG. 1. Snapshots of the configurations at different times t for model B (fractal clusters), where the number of clusters decrease with time. The different panels correspond to (a) $t = 50$, (b) $t = 500$, (c) $t = 5000$, and (d) $t = 25790$. The data are for system size $L = 200$ and initial number of $N = 2000$ particles ($n_0 = 0.05$).

cluster overlapping with other nearby clusters, triggering an avalanche of coalescence events. Model C is motivated from its similar counterpart in the continuum model as considered in Refs. [30,40–43]. Snapshots of a typical time evolution are shown in Fig. 2.

D. Details of simulation

The models are simulated using standard Monte Carlo methods. In all the models, the rates of hopping are modified when the mass of particles change during aggregation. In
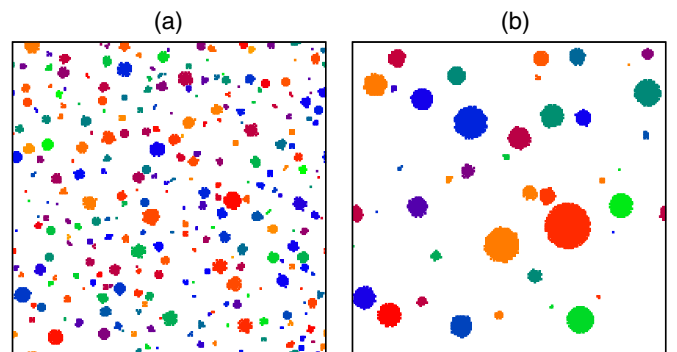

FIG. 2. Snapshots of the configurations at different times t for model C (spherical clusters), where the number of clusters decrease with time. The different panels correspond to (a) $t = 100$ and (b) $t = 500$. The data are for system size $L = 200$ and initial number of $N = 4000$ particles ($n_0 = 0.1$).

addition, the number of particles decrease with aggregation. To make the simulations efficient, we use a variable time step that changes according to the total rate of hopping of all the particles. In particular, we choose a time step such that the probability of one of the particles hopping is exactly equal to 1. This makes the simulations rejection-free.

In models B and C, where extended clusters hop as a single unit, we identify the different clusters and their merging using the well-known Hoshen-Kopelman algorithm [50]. Simulations were carried out for different system sizes varying from $L = 100$ up to $L = 10000$ for all three models and a wide range of number densities n_0. The simulation is continued till all the clusters aggregate together to form the final single cluster. The details of the densities and the lattice sizes used for simulations of the three models are given in Table I.

III. REVIEW OF SCALING THEORY

In this section, we review the scaling theory for BA, described initially in Ref. [35]. Here, we give a scaling argument based on the Smoluchowski equation for aggregation (see Refs. [17,18] for reviews). Different scaling arguments, leading to the same results, may be found in Refs. [41,42]. Let $N(m, t)$ denote the average density of clusters of mass m at time t. $N(m, t)$ evolves in time as

$$\frac{dN(m,t)}{dt} = -N(m,t) \int_0^\infty dm_1 K(m,m_1) N(m_1,t) + \frac{1}{2} \int_0^m dm K(m_1, m-m_1) N(m,t) N(m-m_1, t),$$ (1)

where the kernel $K(m_1, m_2)$ is the rate at which particles of masses m_1 and m_2 collide. The first term on the right-hand side of Eq. (1) describes a loss term where a particle of mass m collides with another particle, while the second term describes a gain term where two particles collide to form a particle of mass m.

We restrict ourselves to homogeneous kernels, which are known to describe many physical systems, examples of which may be found in Refs. [17,18]. Homogeneous kernels have the property

$$K(hm_1, hm_2) = h^\lambda K(m_1, m_2), \quad h > 0,$$ (2)

where λ is called the homogeneity exponent. For $\lambda < 1$, and for large masses and times, it can be shown that Eq. (1) is solved by a $N(m, t)$ which has the scaling form

$$N(m,t) \simeq \frac{1}{t^{2\theta_n}} \Phi\left(\frac{m}{t^{\theta_n}}\right).$$ (3)

For $x \gg 1$, $\Phi(x)$ vanishes exponentially. For $x \ll 1$, $\Phi(x)$ is a power law:

$$\Phi(x) \sim x^\zeta, \quad x \ll 1.$$ (4)

Thus, there are two exponents θ_n and ζ characterizing the mass distribution $N(m, t)$.

The exponent θ_n describes how the mean density of particles $n(t) = \int_m N(m,t) dm$ decreases with time. Integrating Eq. (3), we obtain

$$n(t) \sim t^{-\theta_n}.$$ (5)

The exponent ζ describes the power-law dependence of $N(m, t)$ on mass for small masses:

$$N(m,t) \sim \frac{m^\zeta}{t^{\theta_n(2+\zeta)}}, \quad m \ll t^{\theta_n}.$$ (6)

The dependence of θ_n on the homogeneity exponent λ can be obtained by substituting Eq. (3) into Eq. (1), and is known to be (for example, see Refs. [17,18])

$$\theta_n = \frac{1}{1-\lambda}.$$ (7)

We now focus on the collision kernel that corresponds to BA. Assuming a homogeneous mixture of clusters of all masses, the rate of collision between two masses m_1 and m_2 is proportional to $(r_1 + r_2)^{d-1} |\vec{v}_1 - \vec{v}_2|$, where r_1 and r_2 are the radii of the particles, $\vec{v}_1$ and $\vec{v}_2$ the velocities, and d is the dimension. The relative velocity may be approximated as $|\vec{v}_1 - \vec{v}_2| \approx \sqrt{v_1^2 + v_2^2}$. Thus, the collision kernel for BA may be written as

$$K(m_1, m_2) \propto (r_1 + r_2)^{d-1} \sqrt{v_1^2 + v_2^2}.$$ (8)

To express the radii and velocities in terms of the masses, we assume that the typical speed, v_m, of particles of mass m, scales with mass as

$$v_m^2 \sim m^{-\eta}.$$ (9)

The radii are related to mass though the fractal dimension, d_f, of a cluster:

$$r \propto m^{1/d_f}.$$ (10)

Thus, the kernel in Eq. (8) reduces to

$$K(m_1, m_2) \propto \left[m_1^{1/d_f} + m_2^{1/d_f}\right]^{d-1} \sqrt{m_1^{-\eta} + m_2^{-\eta}}.$$ (11)

This kernel is homogeneous in its arguments with the homogeneity exponent given by

$$\lambda = \frac{d-1}{d_f} - \frac{\eta}{2}.$$ (12)

From Eq. (7), we then obtain

$$\theta_n = \frac{2d_f}{2d_f - 2(d-1) + \eta d_f}.$$ (13)

Another quantity of interest is the mean kinetic energy $e(t)$, defined as

$$e(t) \simeq \int dm \frac{1}{2} m v_m^2 N(m,t).$$ (14)

The energy density decreases in time as a power law $e(t) \sim t^{-\theta_e}$. Substituting $v_m^2 \sim m^{-\eta}$, we obtain the scaling relation:

$$\theta_e = \eta \theta_n.$$ (15)

We now reproduce the results obtained for BA in Ref. [35], which we refer to as the mean-field BA exponents. Here, it is assumed that the clusters that are formed are spherical ($d_f = d$) and that the velocities of the constituent particles of a given cluster are uncorrelated, implying that $\eta = 1$. Substituting these values into Eqs. (13) and (15), we reproduce

the results,

$$\theta_n^{\text{mf}} = \theta_e^{\text{mf}} = \frac{2d}{d+2},\tag{16}$$

where the superscript mf denotes mean field. Note that the main simplifying assumption is that $\eta = 1$. In one dimension, η continues to be 1 as the order of particles is maintained and a cluster made up of m initial neighboring particles will have uncorrelated velocities. However, η need not be 1 in higher dimensions.

We now summarize the scaling theory predictions for the models studied in this paper. For model A, since particles are pointlike objects, we have $r \sim m^0$ or $d_f = \infty$. Similarly, in model C, since clusters are spherical, $d_f = d$, which is spatial dimension itself. We thus obtain

$$\theta_n = \begin{cases} \frac{2}{2+\eta}, & \text{model A} \\ \frac{2d_f}{2d_f - 2 + \eta d_f}, & \text{model B} \\ \frac{2}{1+\eta}, & \text{model C}, \end{cases}\tag{17}$$

with $\theta_e = \eta \theta_n$.

It is useful to have a relation between θ_n and θ_e that does not involve η. This will enable us to verify scaling theory without having to numerically measure the different exponents. Eliminating η, we obtain

$$2\theta_n + \theta_e = 2, \quad \text{model A}$$

$$\frac{2\theta_n}{2\theta_n + \theta_e - 2} = d_f, \quad \text{model B}\tag{18}$$

$$\theta_n + \theta_e = 2, \quad \text{model C}.$$

IV. RESULTS

In this section, we describe the results, obtained from extensive Monte Carlo simulations, for models A, B, and C. For all three models, we will independently determine the exponents θ_n, θ_e, η, and ζ. For model B, the fractal dimension d_f is also measured. Their dependence on number density, the scaling relations between them, as well as deviation from the mean field results, are determined.

A. Model A: Point particles

We first determine θ_n from the power-law decay of the mean density of particles, n, with time t. The data for different initial number density n_0 and initial mean speed v_0 collapse onto one curve when scaled, based on dimensional analysis, according to

$$n(t, n_0) \simeq n_0 f(t n_0 v_0),\tag{19}$$

as shown in Fig. 3. After an initial crossover time $t_c \sim n_0^{-1}$, $n(t)$ decreases as a power law. From the excellent collapse of the data for different n_0 onto one curve, we conclude that the power-law exponent is independent of the initial number density. From fitting a power law to the data, we obtain $\theta_n = 0.633(7)$, which describes the data well over five decades. In the inset of Fig. 3, the compensated curve $t^{\theta_n} n(t)$ is shown for $n_0 = 1$. The mean slope of the curve changes from negative to positive as θ_n varies from 0.626 to 0.640, consistent with our estimate of θ_n from direct measurement.
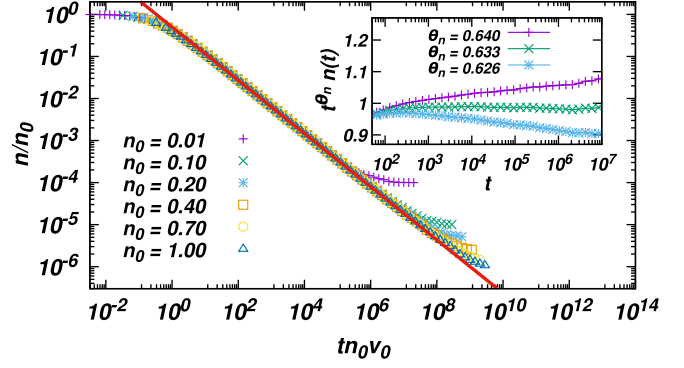

FIG. 3. The data (model A) for mean number density of particles, $n(t)$, for different initial number densities n_0 collapse onto a single curve when $n(t)$ and t are scaled as in Eq. (19). The solid line is a power law $t^{-0.633}$. Inset: The compensated data $n(t)t^{\theta_n}$ is shown for three different choices of θ_n differing by 0.007 for $n_0 = 1.0$. The curve is flat for $\theta_n = 0.633$. The data are obtained for $L = 1000$. All data have been averaged over 300 different initial conditions.

We now numerically determine θ_n using different analyses, both for the sake of consistency as well as for benchmarking different methods that will be more useful in determining exponents for models B and C.

First, we check that the measured value of θ_n is consistent with the mass distribution $N(m, t)$ and then we use finite-size scaling for large times. The dependence of $N(m, t)$ on time and mass are shown in the inset of Fig. 4. When scaled as in Eq. (3) with $\theta_n = 0.633$, the data for different times, that span three decades, collapse onto a single curve (see Fig. 4).

Finally, we examine finite-size effects. For very large times, when the number of clusters is order one, we expect that $n(t) \sim L^{-2}$, where L is the system size. Assuming finite-size scaling, we can write

$$n(t) \simeq \frac{1}{L^2} f_n\left(\frac{t}{L^{2/\theta_n}}\right),\tag{20}$$

where the scaling function $f_n(x) \sim x^{-\theta_n}$ for $x \ll 1$, and $f_n(x) \sim \text{const}$ for $x \gg 1$. The data for $n(t)$ for different L,
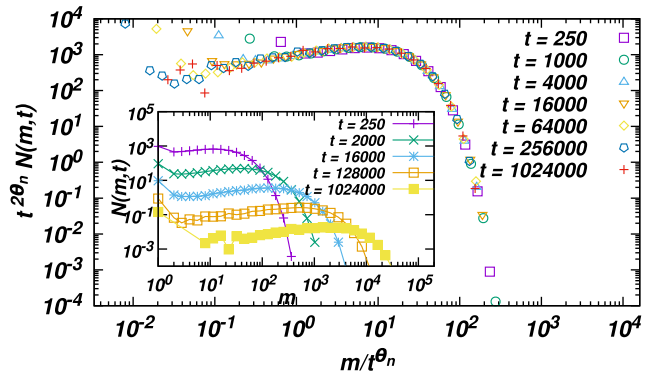

FIG. 4. The mass distribution $N(m, t)$ for different times collapse onto a single curve when scaled as in Eq. (3), with $\theta_n = 0.633$. The data are for model A, with initial number density $n_0 = 1.0$, and system size $L = 1000$ lattice. Inset: The unscaled data for $N(m, t)$ for different times t.
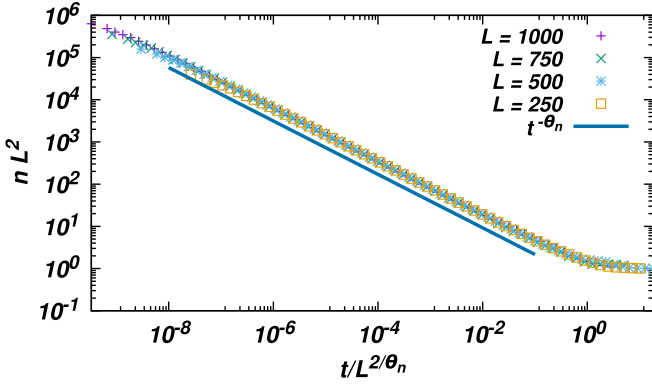
FIG. 5. The number density $n(t)$ for different system sizes L collapse onto a single curve when scaled as in Eq. (20), with $\theta_n = 0.633$. The data are for model A and initial number density $n_0 = 1.0$.

when scaled as in Eq. (20) with $\theta_n = 0.633$, collapse onto a single curve, as shown in Fig. 5. For models B and C, we will find the analysis of the data based on $N(m, t)$ and finite-size scaling very useful for determining the exponents.

We now determine θ_e from the power-law decay of the mean energy density e with time t. The data for energy for different initial number density n_0, initial speed v_0, and initial mean energy e_0 collapse onto one curve when scaled, based on dimensional analysis, as $e(t) \simeq e_0 f_e(t n_0 v_0)$, as can be seen in Fig. 6. After an initial crossover time $t_c \sim n_0^{-1}$, $e(t)$ decreases as a power law. From the excellent data collapse, we conclude that the power-law exponent is independent of the initial number density. From fitting a power law to the data, we obtain $\theta_e = 0.728(5)$, which describes the data well over five decades. In the inset of Fig. 6, the compensated curve $t^{\theta_e} e(t)$ is shown for $n_0 = 1.0$. The mean slope of the curve changes from negative to positive as θ_n varies from 0.723 to 0.733, consistent with our direct measurement of θ_e.

The exponent θ_e can also be determined from finite-size scaling. As for number density, $e(t)$ is expected to obey
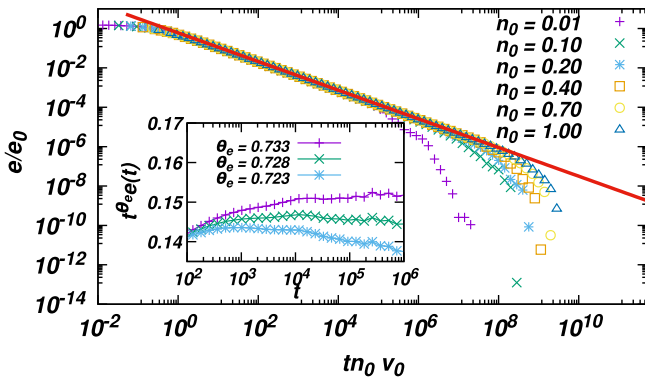

FIG. 6. The data for mean energy density, $e(t)$, at time t for different initial number densities n_0 in model A collapse onto a single curve when $e(t)$ and t are scaled as shown in figure. The solid line is a power law $t^{-0.728}$. Inset: The compensated data $n(t)t^{\theta_e}$ is shown for three different choices of θ_e differing by 0.005 for $n_0 = 1.0$. The curve is flat for $\theta_e = 0.728$. The data are obtained for $L = 1000$. All data have been averaged over 300 different initial conditions.
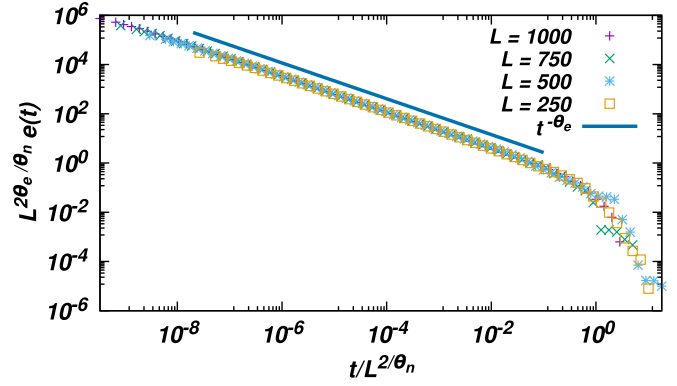

FIG. 7. The mean energy $e(t)$ for different system sizes L collapse onto a single curve when scaled as in Eq. (21), with $\theta_n = 0.633$ and $\theta_e = 0.728$. The data are for model A and initial number density $n_0 = 1.0$.

finite-size scaling of the form

$$e(t) \simeq \frac{1}{L^{2\theta_e/\theta_n}} f_e\left(\frac{t}{L^{2/\theta_n}}\right), \tag{21}$$

where the scaling function $f_e(x) \sim x^{-\theta_e}$ for $x \ll 1$, and $f_e(x) \sim$ const for $x \gg 1$. The simulation data for different L collapse onto a single curve (see Fig. 7) when $e(t)$ and t are scaled as in Eq. (21) with $\theta_n = 0.633$ and $\theta_e = 0.728$. The power law extends over four decades.

We now determine the exponent η relating the scaling of velocity with mass as $v_m^2 \sim m^{-\eta}$ [see Eq. (9)]. As seen from Fig. 8, $\langle v^2 \rangle$ for a fixed mass scales as a power law with m. We obtain $\eta = 1.1505(3)$.

Note that η is not an independent exponent, but related to θ_n and θ_e through scaling theory, to be $\eta = \theta_e/\theta_n$ [see Eq. (17)]. From the measured values of $\theta_e = 0.728$ and $\theta_n = 0.633$, we obtain $\eta = 1.15$, consistent with the value from direct measurement $\eta = 1.1505(3)$, thus providing support for the correctness of scaling theory.

We now provide a more direct evidence of scaling theory being correct. From Eqs. (17) and (15), we obtain, by
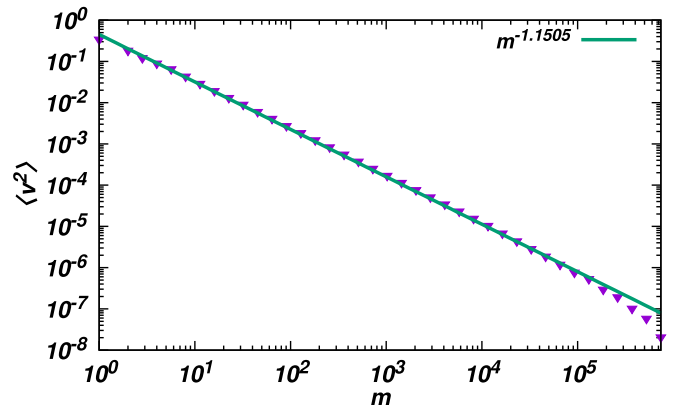

FIG. 8. The variation of the mean-square velocity $\langle v^2 \rangle$ with mass m. The solid line is power law $t^{-\eta}$ with $\eta = -1.1505$. The data are for model A, with $n_0 = 1.0$ and system size $L = 1000$.
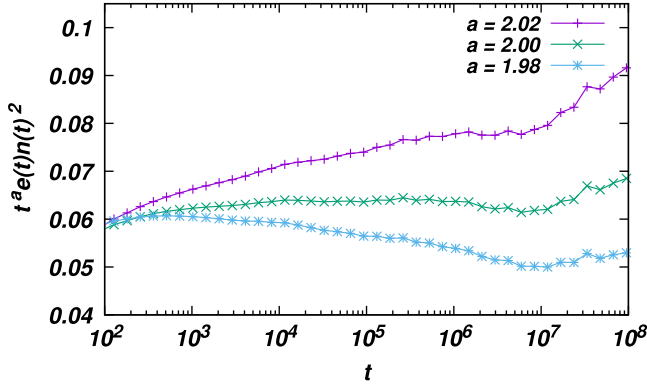
FIG. 9. The variation of $t^a n^2(t)e(t)$ with time t for three different values of a close to 2. The compensated curve is horizontal for $a = 2.0$, validating the scaling relation in Eq. (18). The data are for model A, with initial number density $n_0 = 1.0$ and system size $L = 1000$.

eliminating η, a relation between θ_e and θ_n as given in Eq. (18). If this relation is true, it implies that $t^2 n^2(t)e(t)$ should not depend on time t. In Fig. 9, we show the variation of $t^a n^2(t)e(t)$ with $a = 1.98, 2.00, 2.02$. It is clear that only for $a = 2.0$ is the curve horizontal. This gives us a way of validating the scaling relations without the need to measure any exponent directly.

Finally, we determine the exponent ζ defined in Eq. (6) for small masses: $N(m, t) \sim m^\zeta t^{-\theta_n(2+\zeta)}$. Note that ζ is not related to θ_n or θ_e and is an independent exponent. To determine ζ, we study the temporal behavior of $N(m, t)$ for fixed mass $m = 2, 4, 8, 12, 16$. As shown in Fig. 10, the data for the different masses for large times collapse onto one curve when $N(m, t)$ is scaled as $N(m, t)/m^\zeta$, with $\zeta = 0.270(5)$. We additionally check that the scaled data are consistent with the power law $t^{-\theta_n(2+\zeta)}$ for large times.

The numerically obtained values of the exponents for model A are summarized in Table II.

B. Model B: Fractal clusters

In this subsection, we determine the exponents θ_n, θ_e, η, and ζ for model B. We first show that the clusters in model
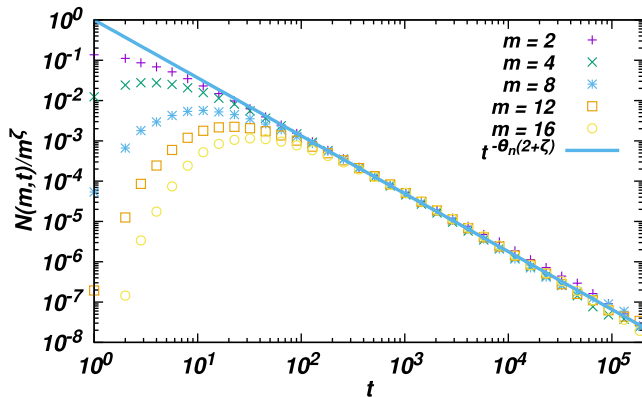

FIG. 10. The data for $N(m, t)$ for different masses for large times collapse onto one curve when the number density is scaled as $N(m, t)/m^\zeta$ with $\zeta = 0.270$. The solid line is a power law $t^{-\theta_n(2+\zeta)}$ with $\theta_n = 0.633$. The data are for model A, with initial number density $n_0 = 1.0$.
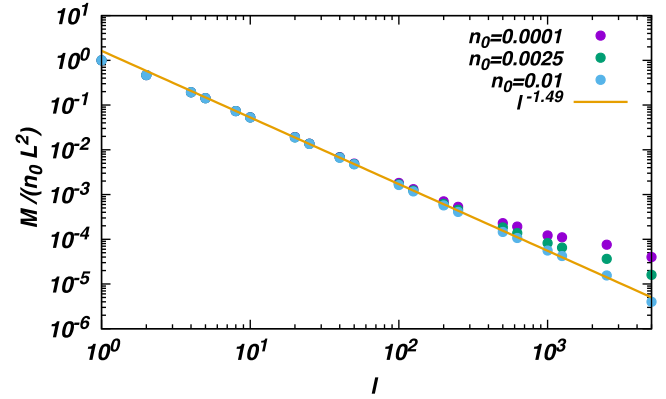

FIG. 11. Determination of the fractal dimension of the largest cluster in model B using the box-counting method. The number of nonempty boxes, M, varies with the size ℓ of the boxes used to tile the lattice as $M \sim \ell^{-d_f}$. We find $d_f \approx 1.49(3)$ (power law shown by solid line) irrespective of the initial density. The data are for $L = 5000$.

B are fractal with a fractal dimension, d_f, that lies between 1 and 2. To determine d_f, we consider the final cluster in each of the simulations for a given initial number density n_0. d_f of this cluster is measured using the box-counting method [51]. In this method, the lattice is tiled with square boxes of length ℓ. Let M be the number of nonempty boxes. Then $M \sim \ell^{-d_f}$. The results for three different n_0 are shown in Fig. 11. The data for different n_0 fall on top of each other for intermediate box sizes. The same is true for other n_0 and we conclude that d_f is independent of n_0. We estimate d_f to be 1.49(3).

Consider now the decay of the density of particles $n(t)$ with time t. We find that for model B, it is difficult to accurately determine θ_n directly from the data for $n(t)$ because of strong crossover effects. This can be seen from Fig. 12 where the variation of $n(t)$ with t is shown for two different initial densities $n_0 = 0.00125$ and $n_0 = 0.01$. The data for the two densities overlap for short times but deviate for larger
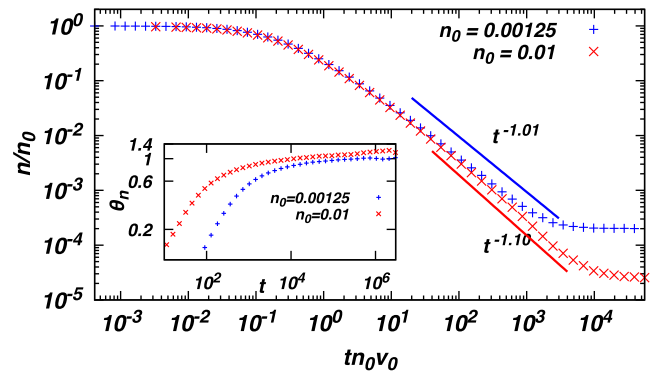

FIG. 12. The variation of the mean density of clusters $n(t)$ in model B with time t is shown for two different initial densities. The exponents for the power laws, shown by solid lines, have been obtained from finite-size scaling. Inset: The time-dependent exponent θ_n obtained from $\theta_n = -d \ln n(t)/d \ln t$ is shown. θ_n saturates for the larger initial densities only at late times. Data are for $L = 2000$ and averaged over 300 different initial conditions.
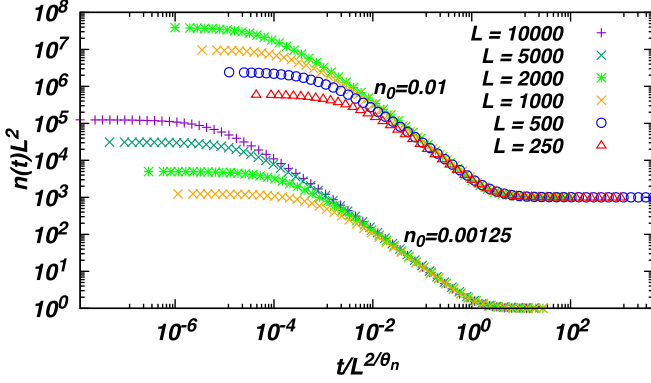
FIG. 13. Finite-size scaling of $n(t)$ for model B: The number density $n(t)$ for different system sizes L collapse onto a single curve when scaled as in Eq. (20), with $\theta_n = 1.01$ and $\theta_n = 1.10$ for the initial densities $n_0 = 0.00125$ and $n_0 = 0.01$, respectively. The data for $n_0 = 0.01$ has been shifted for clarity.

times. The solid lines, which are the estimates for θ_n from finite-size scaling (to be discussed below) match with the data only for late times. The convergence to the asymptotic answer can also be seen from measuring the instantaneous slope $\theta_n = -d \ln n(t)/d \ln t$ for each time (see inset of Fig. 12). We find that the exponent θ_n saturates only at late times for the larger initial densities. We find that the same issue is present for the temporal decay of energy $e(t)$, making it difficult to also measure θ_e directly.

We determine θ_n from finite-size scaling. For finite systems, $n(t)$ has the finite-size scaling form given in Eq. (20), namely, $n(t) \simeq L^{-2} f_n(t/L^{2/\theta_n})$. In Fig. 13, we show the results for two representative initial densities $n_0 = 0.00125$ and $n_0 = 0.01$. The data for different L, when scaled as in Eq. (20), collapse onto a single curve with $\theta_n = 1.01(1)$ for $n_0 = 0.00125$ and $\theta_n = 1.10(1)$ for $n_0 = 0.01$. The results for the other n_0 are listed in Table III, based on which we conclude that θ_n depends on n_0 and converges to $\theta_n = 1$ as $n_0 \to 0$. We also check that the same value of θ_n leads to the collapse of the data for $N(m, t)$ for different times when scaled as in Eq. (3).

The limiting value of $\theta_n = 1$ for $n_0 \to 0$ coincides with $\theta_n^{mf} = 1$. However, it is not clear whether the mean-field result is obtained because correlations vanish. We check for correlations by measuring the exponent η. In Fig. 14, we show the dependence of the mean-squared velocity on the mass m for two initial densities. The power-law dependence extends over three decades and we obtain exponents that depend on the initial density n_0 with $\eta = 1.293(4)$ for $n_0 = 0.00125$ and $\eta = 1.204(3)$ for $n_0 = 0.01$. The results for other n_0 are listed in Table III, based on which we conclude that η also depends on n_0 and differs significantly from one for small n_0. However, as n_0 increases, we find that $\eta \to 1$.

Since it is difficult to measure θ_e directly from $e(t)$, we estimate θ_e using the scaling relation $\theta_e = \eta \theta_n$ [see Eq. (15)]. To check for consistency, we confirm that for this choice of θ_e, the data for different system sizes collapse onto one curve when $e(t)$ and t are scaled using finite-size scaling as described in Eq. (21). The data collapse for two different n_0, shown in Fig. 15, is satisfactory. The results of θ_e for different n_0 are listed in Table III.
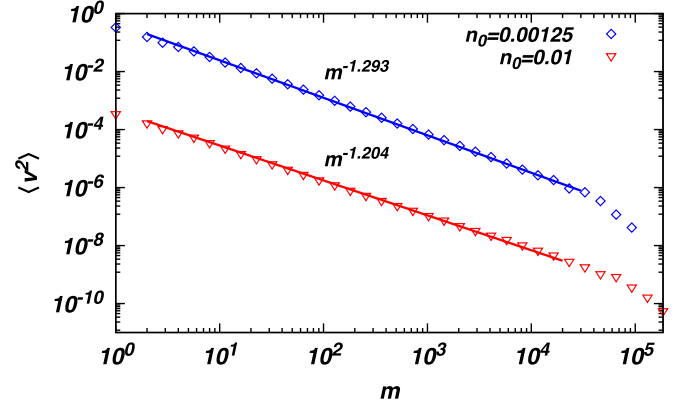

FIG. 14. The variation of the mean-square velocity $\langle v^2 \rangle$ with mass m for different initial densities. The solid lines are power laws $m^{-\eta}$ with $\eta = 1.293(4)$ for $n_0 = 0.00125$ and $\eta = 1.204(3)$ for $n_0 = 0.01$. The data are for model B with system sizes $L = 10000$ for $n_0 = 0.00125$ and $L = 5000$ for $n_0 = 0.01$. The data for $n_0 = 0.01$ has been shifted for clarity.

Finally, we determine the exponent ζ defined in Eq. (6) for small masses. Similar to model A, to determine ζ, we study the temporal behavior of $N(m, t)$ for fixed mass $m = 2, 4, 8, 12, 16$. Here, we illustrate the behavior of ζ for two different initial densities. As shown in Fig. 16, the data for the different masses collapse onto one curve for the respective initial densities when $N(m, t)$ is scaled as $N(m, t)/m^\zeta$, with $\zeta = -0.4229(6)$ for $n_0 = 0.00125$ and $\zeta = -0.538(24)$ for $n_0 = 0.01$. As an additional check, the scaled data are consistent with the power law with an exponent $t^{-\theta_n(2+\zeta)}$. Thus, the exponent ζ is dependent on the initial density n_0. Also, they are negative, as compared to model A where the exponent is positive.

The results for the exponents θ_n, θ_e, η, d_f, and ζ are summarized in Table III and their dependence on number density n_0 is shown in Fig. 17. For higher densities, it is difficult to get the exponents θ_n and hence θ_e due to increasing finite-size effects. However, the exponent η can be calculated
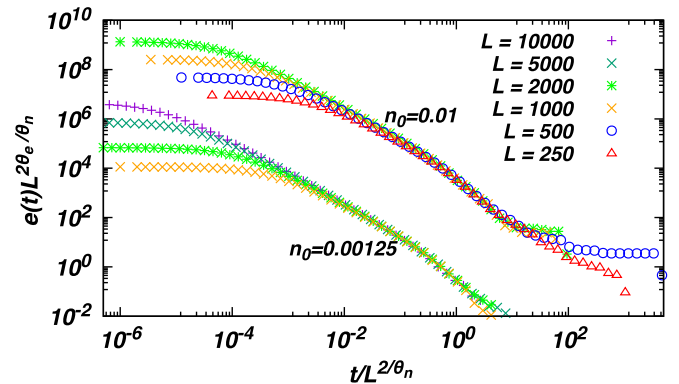

FIG. 15. Finite-size scaling of $e(t)$ for model B: The mean energy $e(t)$ for different system sizes L collapse onto a single curve when scaled as in Eq. (21). Results for two different densities $n_0 = 0.00125$ and $n_0 = 0.01$ (vertically shifted for visualization) is shown with θ_n obtained using finite-size scaling [Eq. (20)] whereas θ_e is obtained using the hyperscaling relation [Eq. (15)].
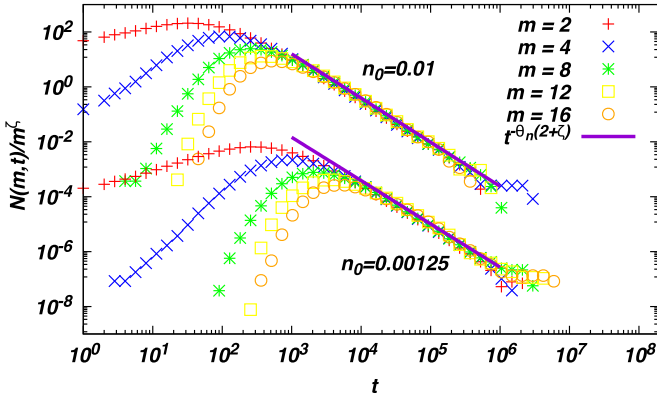
FIG. 16. The data for $N(m,t)$ in model B for fixed masses collapse onto one curve when the number density is scaled as $N(m,t)/m^\zeta$ with $\zeta = -0.422(6)$ for $n_0 = 0.00125$ whereas $\zeta = -0.538(24)$ for $n_0 = 0.01$. The solid line is a power law $t^{-\theta_n(2+\zeta)}$, with θ_n taking values 1.01 and 1.10 for the initial densities 0.00125 and 0.01 (vertically shifted for visualization), respectively.

for the densities larger than 0.01. From Table III, we observe that, when $n_0 \to 0$, the exponents tend to the limiting values $\theta_n \to 1$, $\eta \to 1.3$, and $\theta_e \to 1.3$. When the density increases, we find that $\eta \to 1$, thus approaching its mean-field value $\eta^{\mathrm{mf}} = 1$. We conclude that velocity correlations vanish as density increases. We note that in model B, there is no avalanche of coalescence events caused due to two clusters colliding. We also verify that the exponents satisfy the hyperscaling relation given by Eq. (18). In Table III, the fractal dimension determined numerically is compared with that obtained by Eq. (18) [see columns 5 and 6]. For all densities, the values are equal within error bars, thus consistent with the scaling theory.

C. Model C: Spherical clusters

We now determine the exponents θ_n, θ_e, η, and ζ for model C. We first show that the exponent θ_n depends on initial densities n_0. Figure 18 shows the variation of $n(t)$ with time t for two different initial densities, one small and one large. The time-dependent $\theta_n = -d \ln n(t)/d \ln t$, shown in
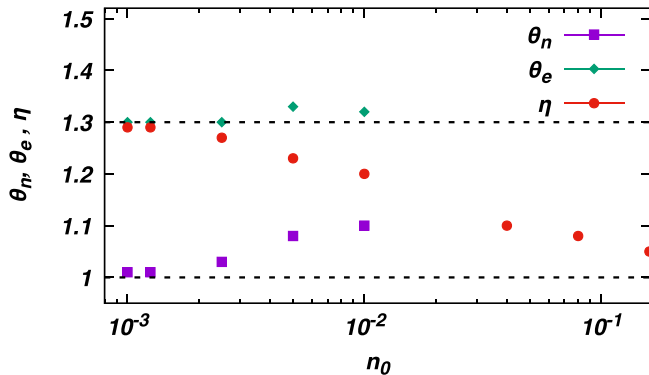

FIG. 18. The variation of the mean density of clusters $n(t)$ in model C with time t is shown for two different initial densities. The exponents for the power laws, shown by solid lines, have been obtained from finite-size scaling. Inset: The time-dependent exponent θ_n obtained from $\theta_n = -d \ln n(t)/d \ln t$ is shown. θ_n saturates for the larger initial densities only at late times. The dashed lines are the reference for the exponents 0.83 and 0.93. Data are for $L = 2000$ and averaged over 300 different initial conditions.

the inset, saturates at different values for the different initial densities. Like for model B, it is difficult to measure θ_n directly as $n(t)$ shows strong crossover effects. For this reason, we determine θ_n from finite-size scaling (see below) following which we obtain $\theta_n = 0.83$ for $n_0 = 0.0001$ and $\theta_n = 0.93$ for $n_0 = 0.16$. The exponents obtained from finite-size scaling are shown in Fig. 18 for comparison and they describe the data for large times well.

We determine the exponent θ_n using the finite-size scaling $n(t) \simeq L^{-2} f_n(t/L^{2/\theta_n})$ [see Eq. (20)]. Two representative cases are shown in Fig. 19. The data of $n(t)$ for different L, when scaled as in Eq. (20) collapse onto a single curve for $\theta_n = 0.83$ for $n_0 = 0.001$ and $\theta_n = 0.93$ for $n_0 = 0.16$. The results for other n_0 are listed in Table IV, based on which we conclude that θ_n depends on n_0 and increases to the mean-field result $\theta_n^{\mathrm{mf}} = 1$ with increasing n_0. We also check that the same value of θ_n leads to the collapse of the data for $N(m,t)$ for different times when scaled as in Eq. (3).

FIG. 17. The variation of the exponents θ_n, θ_e, and η are shown as function of the initial density n_0. The data are for model B. θ_n and θ_e approach an asymptotic limit 1.0 and 1.3, respectively, for lowest densities. The exponent $\eta \approx 1.3$ in the low density limit and approaches the mean-field result ($\eta = 1$) for higher density.
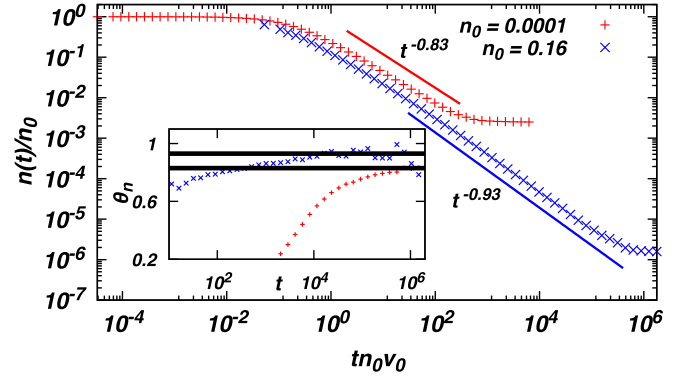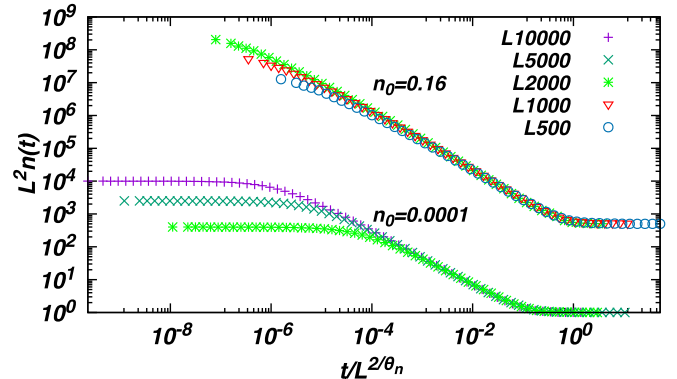

FIG. 19. Finite size scaling of $n(t)$ for model C: The number density $n(t)$ for different system sizes L collapse onto a single curve when scaled as in Eq. (20), with $\theta_n = 0.83(4)$ and $\theta_n = 0.93(5)$ for the initial densities $n_0 = 0.0001$ and $n_0 = 0.16$, respectively. The data for $n_0 = 0.16$ has been shifted for clarity.
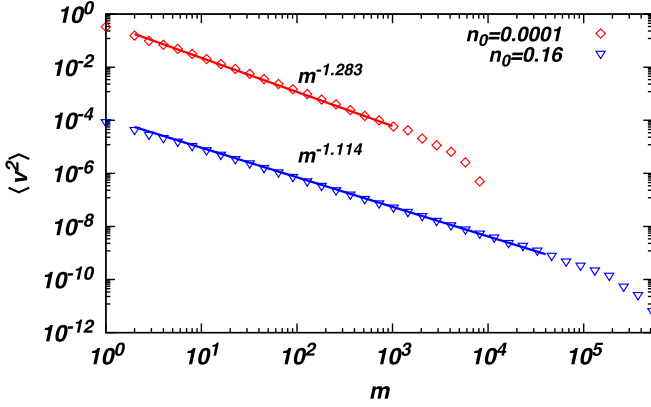
FIG. 20. The variation of the mean-square velocity $\langle v^2 \rangle$ plotted as function of mass m for different initial densities. The solid lines are power laws $m^{-\eta}$ with $\eta = 1.283(13)$ and $\eta = 1.114(2)$ for $n_0 = 0.0001$ and $n_0 = 0.16$, respectively. The data are for model C with system sizes $L = 10000$ and $L = 2000$ for the densities $n_0 = 0.0001$ and $n_0 = 0.16$, respectively. The data for $n_0 = 0.16$ has been shifted for clarity.

It is possible that the mean-field result is obtained at higher n_0 because the correlations vanish. Two representative cases are shown in Fig. 20. We find that η depends on the initial density n_0 with $\eta = 1.283(13)$ for $n_0 = 0.0001$ and $\eta = 1.114(2)$ for $n_0 = 0.16$. The results for other n_0 are listed in Table IV and show that η decreases to its mean field prediction $\eta^{\mathrm{mf}} = 1$ as density increases.

We find that it is difficult to measure θ_e directly from the power-law decay of $e(t)$. Hence, we measure θ_e using the scaling relation, $\theta_e = \eta \theta_n$ [see Eq. (15)]. To check for the consistency of the result for θ_e obtained using the scaling relation [Eq. (15)], we confirm that for this choice of θ_e, the data for different system sizes can be collapsed onto one curve using finite-size scaling $e(t) \simeq L^{-2\theta_e/\theta_n} f_e(t/L^{2/\theta_n})$ [see Eq. (21)]. The data collapse is satisfactory as shown in Fig. 21 for the two different n_0. The results of θ_e for different n_0 are listed in
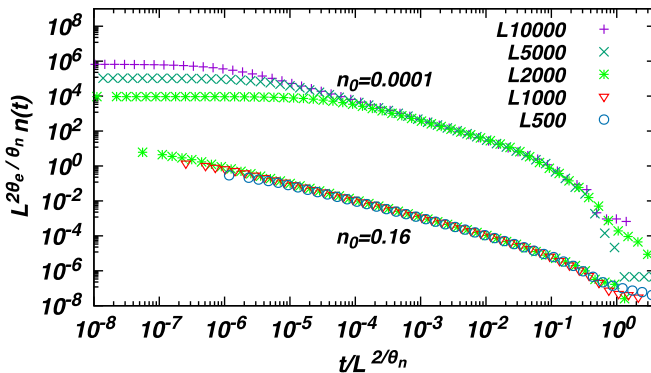

FIG. 21. Finite-size scaling of $e(t)$ for model C: The mean energy density $e(t)$ for different system sizes L collapse onto a single curve when scaled as in Eq. (21). Results for two different densities $n_0 = 0.0001$ and $n_0 = 0.16$ are shown with θ_n obtained using finite-size scaling [Eq. (20)] whereas θ_e is obtained using the hyperscaling relation [Eq. (15)]. The data for $n_0 = 0.0001$ has been shifted for clarity.
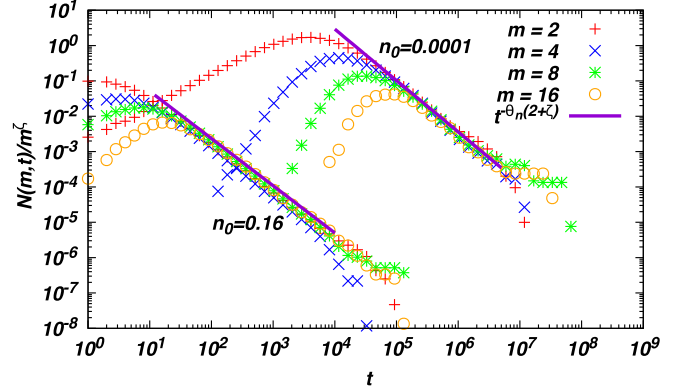

FIG. 22. The data for $N(m, t)$ in model C for fixed masses collapse onto one curve when the number density is scaled as $N(m, t)/m^\zeta$, with $\zeta = -0.248(26)$ for $n_0 = 0.0001$ whereas $\zeta = -0.563(10)$ for $n_0 = 0.16$. The solid line is a power law $t^{-\theta_n(2+\zeta)}$ with θ_n as 0.83 and 0.93 for the initial densities 0.0001 and 0.16, respectively. The data for $n_0 = 0.0001$ has been shifted for clarity.

Table IV, which shows that θ_e is close to the mean-field limit, $\theta_e^{\mathrm{mf}} = 1$ for all n_0.

Finally, we determine the exponent ζ [defined in Eq. (6)] for small masses. To determine ζ, we study the temporal behavior of $N(m, t)$ for fixed mass $m = 2, 4, 8, 16$. Here, we illustrate the behavior of ζ for two different initial densities. As shown in Fig. 22, the data for the different masses collapse onto one curve for the respective initial densities when $N(m, t)$ is scaled as $N(m, t)/m^\zeta$, with $\zeta = -0.248(26)$ for $n_0 = 0.0001$ and $\zeta = -0.563(10)$ for $n_0 = 0.16$. As an additional check, the scaled data are consistent with the power law with an exponent $t^{-\theta_n(2+\zeta)}$. The results of ζ for other densities are listed in Table IV. We conclude that ζ is strongly dependent on n_0.

We find that the exponents θ_n, θ_e, η, and ζ are density dependent [see Table IV and Fig. 23(a)]. θ_n increases with the increase in density and approaches the mean-field predictions $\theta_n^{\mathrm{mf}} = 1$. An opposite trend is observed in the variation of exponent η with density where it decreases with the increase in initial density but, approaches the mean-field prediction $\eta^{\mathrm{mf}} = 1$ with the increase in density. On the other hand, θ_e has a rather weak dependence on the initial density and is always close to the mean-field result $\theta_e^{\mathrm{mf}} = 1$ irrespective of the initial density. We compare our results with those for BA in the continuum [41,43] in Fig. 23(b). We find that the data are in good agreement, suggesting that the stochasticity introduced in the temporal evolution of the lattice model is not relevant.

V. CONCLUSION

In this paper, we studied the problem of BA in two dimensions using three different lattice models. In all three models, particles move, on an average, in a straight line and undergo momentum-conserving aggregation on contact. The three models differ in the shape of the particles. In model A, the particles are point sized and occupy a single lattice site. In model B, the shape of the aggregate is the combined shape of
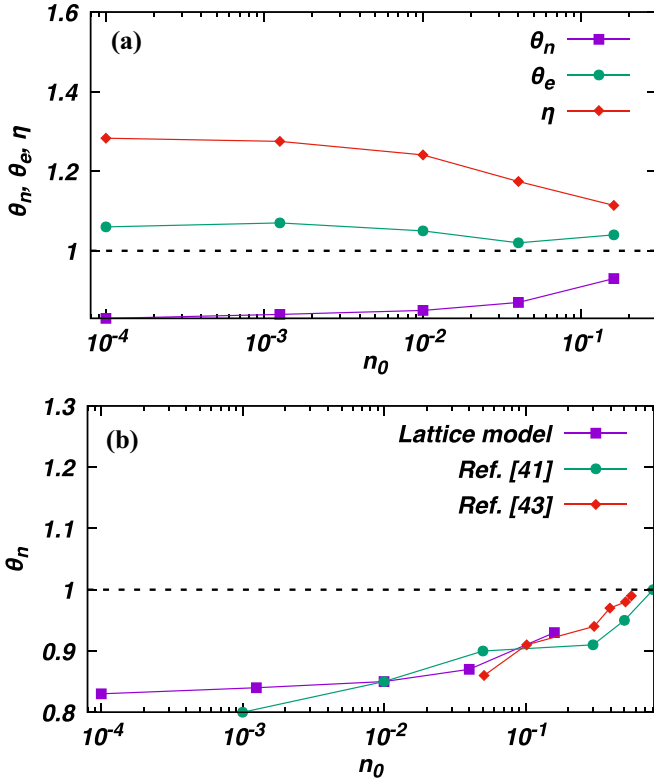
FIG. 23. (a) The variation of the exponents θ_n, θ_e, and η with initial density, n_0, for model C. The horizontal dotted line is the mean-field prediction, $\theta_n^{\mathrm{mf}} = \theta_e^{\mathrm{mf}} = \eta^{\mathrm{mf}} = 1$. (b) Comparison of the exponent θ_n with results of earlier simulations of BA in the continuum [41,43].

the two aggregating particles at the time of collision, and is a fractal. In model C, the shape of the particles are spherical, to the closest lattice approximation. For the three models, from large-scale Monte Carlo simulations, we determine the exponents characterizing the power-law decay of the number density of particles, the mean energy, the fractal dimension, the correlation between the velocities of the particles constituting an aggregate, and the scaling function for the mass distribution. The results for the three models are summarized in Table II (model A), Table III and Fig. 17 (model B), Table IV and Fig. 23 (model C).

We find that the values of the exponents are independent of the initial number density only for model A. For models B and C, the exponents are weakly dependent on the initial number density, making them nonuniversal. The fractal dimension in model B is, however, independent of the initial number density, within the numerical accuracy that we could achieve. In model C, the trends in the dependence of the exponents on n_0 are consistent with the corresponding simulations for spherical particles in the continuum [30,40–43]. While the exponent θ_n matches closely with the continuum results [see Fig. 23(b)], we find that the numerical values of the exponent θ_e are less than the continuum result [43] and approaches the mean-field result faster. This discrepancy could be due to difficulties in measuring θ_e accurately due to strong crossovers seen in the data. We have shown that the results for the exponents in all models, irrespective of its dependence on n_0, satisfy the hyperscaling relations derived from scaling theory.

The fractal dimension of clusters formed by aggregation is of interest in many experiments (for example, see Refs. [5,44–47]). While it is to be expected that the exponents θ_n and θ_e will depend on the nature of transport and the shapes of the clusters, it is not clear whether the fractal dimension depends on transport. Fractal dimension of the cluster in two-dimensional DLA models, where clusters grow from a nucleating center, show $d_f \simeq 1.70$ [52,53]. However, fractal dimension of clusters, when there is no nucleating center but all the aggregates undergo diffusive motion, is different from that of DLA. In the case when the diffusion constant of larger masses decreases with mass or is mass independent, d_f has been been shown to be in the range $d_f \simeq 1.38 - 1.52$ [49,54,55]. This result is close to our result for BA (model B) for which we found $d_f \simeq 1.49$. While close, it is not clear whether the fractal dimension is different for the diffusive and ballistic models. The value 1.49 is very close to that observed in sprays (1.54) [47], and cells (1.5) [46]. It would be interesting to explore this connection further as well as understand the dependence of the fractal dimension on different mass-dependent velocities, especially the limit where larger masses move faster.

The mean-field approximation assumes that the velocities of the particles forming a cluster are uncorrelated. The correlations are characterized by the power-law dependence of the speed on the mass of the aggregate: $\langle v^2(m) \rangle \sim m^{-\eta}$, with $\eta^{\mathrm{mf}} = 1$. Earlier simulations of spherical particles in the continuum show that η decreases to $\eta = \eta^{\mathrm{mf}}$ as the initial number density of particles, n_0, is increased [30,40–43]. This lack of correlation was attributed to the increased avalanche of coagulation events that occur due to the overlap of a newly created spherical particle with already existing particles as the number density is increased. In this paper, we determined η for the three models. For model A, we find that $\eta \approx 1.15$ is independent of n_0 and hence there is no limit in which velocities become uncorrelated. For models B and C, we find that $\eta \to \eta^{\mathrm{mf}}$ with increasing n_0 (see Tables III and IV). However, in model B there is no avalanche of collisions while model C has an avalanche of collisions. Thus, contrary to earlier conjecture, the avalanche of collisions cannot be a necessary condition for velocities to become uncorrelated.

In contrast to BA in the continuum where the dynamics is deterministic, the temporal evolution in the lattice models is stochastic. Each particle moves in a straight line only on an average. In the continuum models, stochasticity enters only through the initial conditions. However, for BA in one dimension, it has been shown that the stochasticity in the dynamics not only does not affect scaling laws, the lattice models reproduce many details of the trajectory like shock positions for the same initial conditions [24,48]. For model C, we find that the results for θ_n match with the earlier continuum results in two dimensions for all n_0. We thus conclude that stochasticity in the initial conditions dominate the fluctuations induced by the dynamics. This is in sharp contrast to diffusive systems where diffusive fluctuations dominate randomness in initial conditions.

For all the three models, we measure the exponent ζ [see definition in Eq. (6)], which characterizes the behavior of smaller mass aggregates. The exponent ζ is not easily

obtained from scaling arguments and for the corresponding diffusive problem requires renormalization group calculations [56–58]. For model A, we find that ζ is positive, implying that there is a typical time-dependent mass. This is in contrast to point particles in one dimension where the mass distribution is a power law. For models B and C, we find that ζ is dependent on n_0. However, it is negative for all values of n_0, implying that the mass distribution is a power law in mass for a given time. In addition, it would be interesting to study the effect of spatial effects and mass-mass correlations on the exponent ζ by comparing the results obtained from the Monte Carlo simulations with the results from direct numerical solution of the Smoluchowski equation, which ignores all correlations.

[1] G. M. Whitesides and B. Grzybowski, Self-assembly at all scales, Science **295**, 2418 (2002).

[2] G. M. Hidy and J. R. Brock, *Dynamics of Aerocolloidal Systems* (Pergamon Press, Oxford, 1970).

[3] R. Drake, *Topics in Current Aerosol Research*, *Part 2* (Pergamon, Oxford, 1972), Vol. 3.

[4] S. K. Friedlander, *Smoke, Dust, and Haze* (Oxford University Press, New York, 2000), Vol. 198.

[5] C. M. Sorensen, J. Yon, F. Liu, J. Maughan, W. R. Heinson, and M. J. Berg, Light scattering and absorption by fractal aggregates including soot, J. Quant. Spectrosc. Radiat. Transfer **217**, 459 (2018).

[6] W. H. Stockmayer, Theory of molecular size distribution and gel formation in branched-chain polymers, J. Chem. Phys. **11**, 45 (1943).

[7] H. R. Pruppacher and J. D. Klett, *Microphysics of Clouds and Precipitation*, 2nd ed. (Kluwer Academic Publishers, Dordrecht, 1997).

[8] A. N. Ganesh, E. N. Donders, B. K. Shoichet, and M. S. Shoichet, Colloidal aggregation: From screening nuisance to formulation nuance, Nano Today **19**, 188 (2018).

[9] M. H. Lee, On the validity of the coagulation equation and the nature of runaway growth, Icarus **143**, 74 (2000).

[10] L. Esposito, *Planetary Rings* (Cambridge University Press, Cambridge, UK, 2006), Vol. 4.

[11] N. Brilliantov, P. Krapivsky, A. Bodrova, F. Spahn, H. Hayakawa, V. Stadnichuk, and J. Schmidt, Size distribution of particles in Saturn's rings from aggregation and fragmentation, Proc. Natl. Acad. Sci. USA **112**, 9536 (2015).

[12] J. Blum, Dust evolution in protoplanetary discs and the formation of planetesimals, Space Sci. Rev. **214**, 52 (2018).

[13] C. Connaughton, A. Dutta, R. Rajesh, N. Siddharth, and O. Zaboronski, Stationary mass distribution and nonlocality in models of coalescence and shattering, Phys. Rev. E **97**, 022137 (2018).

[14] A. M. Tom, R. Rajesh, and S. Vemparala, Aggregation dynamics of rigid polyelectrolytes, J. Chem. Phys. **144**, 034904 (2016).

[15] A. M. Tom, R. Rajesh, and S. Vemparala, Aggregation of flexible polyelectrolytes: Phase diagram and dynamics, J. Chem. Phys. **147**, 144903 (2017).

[16] S. N. Dorogovtsev and J. F. Mendes, Evolution of networks, Adv. Phys. **51**, 1079 (2002).

[17] F. Leyvraz, Scaling theory and exactly solved models in the kinetics of irreversible aggregation, Phys. Rep. **383**, 95 (2003).

[18] C. Connaughton, R. Rajesh, and O. Zaboronski, Kinetics of cluster-cluster aggregation, in *Handbook of Nanophysics: Clusters and Fullerenes*, edited by K. D. Sattler (Taylor and Francis, Boca Raton, USA, 2010).

[19] D. J. Aldous, Deterministic and stochastic models for coalescence (aggregation and coagulation): A review of the mean-field theory for probabilists, Bernoulli **5**, 3 (1999).

[20] S. Kida, Asymptotic properties of burgers turbulence, J. Fluid Mech. **93**, 337 (1979).

[21] L. Frachebourg, P. A. Martin, and J. Piasecki, Ballistic aggregation: A solvable model of irreversible many particles dynamics, Physica A **279**, 69 (2000).

[22] R. Tribe and O. Zaboronski, On the large time asymptotics of decaying burgers turbulence, Commun. Math. Phys. **212**, 415 (2000).

[23] J. M. Burgers, *The Nonlinear Diffusion Equation: Asymptotic Solutions and Statistical Problems* (Springer Science & Business Media, Dordrecht, 2013).

[24] S. Dey, D. Das, and R. Rajesh, Lattice models for ballistic aggregation in one dimension, Europhys. Lett. **93**, 44001 (2011).

[25] H. Takayasu, Steady-state distribution of generalized aggregation system with injection, Phys. Rev. Lett. **63**, 2563 (1989).

[26] C. Connaughton, R. Rajesh, and O. Zaboronski, Breakdown of kolmogorov scaling in models of cluster aggregation, Phys. Rev. Lett. **94**, 194503 (2005).

[27] C. Connaughton, R. Rajesh, and O. Zaboronski, Cluster–cluster aggregation as an analogue of a turbulent cascade: Kolmogorov phenomenology, scaling laws and the breakdown of self-similarity, Physica D **222**, 97 (2006).

[28] E. Ben-Naim, S. Y. Chen, G. D. Doolen, and S. Redner, Shock-like dynamics of inelastic gases, Phys. Rev. Lett. **83**, 4069 (1999).

[29] X. Nie, E. Ben-Naim, and S. Chen, Dynamics of freely cooling granular gases, Phys. Rev. Lett. **89**, 204301 (2002).

[30] S. N. Pathak, Z. Jabeen, D. Das, and R. Rajesh, Energy decay in three-dimensional freely cooling granular gas, Phys. Rev. Lett. **112**, 038001 (2014).

[31] M. Shinde, D. Das, and R. Rajesh, Equivalence of the freely cooling granular gas to the sticky gas, Phys. Rev. E **79**, 021303 (2009).

[32] R. Dandekar, S. Chakraborti, and R. Rajesh, Hard core run and tumble particles on a one-dimensional lattice, Phys. Rev. E **102**, 062111 (2020).

[33] G. Wetherill, *The Formation and Evolution of Planetary Systems* (Cambridge University Press, Cambridge, 1988).

[34] P. Meakin, Fractal aggregates in geophysics, Rev. Geophys. **29**, 317 (1991).

[35] G. F. Carnevale, Y. Pomeau, and W. R. Young, Statistics of ballistic agglomeration, Phys. Rev. Lett. **64**, 2913 (1990).

[36] S. N. Pathak, D. Das, and R. Rajesh, Inhomogeneous cooling of the rough granular gas in two dimensions, Europhys. Lett. **107**, 44001 (2014).

[37] J. Piasecki, Universal distribution of masses in a one-dimensional sticky gas, Physica A **190**, 95 (1992).

[38] L. Frachebourg, Exact solution of the one-dimensional ballistic aggregation, Phys. Rev. Lett. **82**, 1502 (1999).

[39] E. Ben-Naim and P. Krapivsky, Stochastic aggregation: scaling properties, J. Phys. A: Math. Gen. **33**, 5477 (2000).

[40] E. Trizac and J.-P. Hansen, Dynamic scaling behavior of ballistic coalescence, Phys. Rev. Lett. **74**, 4114 (1995).

[41] E. Trizac and J.-P. Hansen, Dynamics and growth of particles undergoing ballistic coalescence, J. Stat. Phys. **82**, 1345 (1996).

[42] E. Trizac and P. L. Krapivsky, Correlations in ballistic processes, Phys. Rev. Lett. **91**, 218302 (2003).

[43] S. Paul and S. K. Das, Dimension dependence of clustering dynamics in models of ballistic aggregation and freely cooling granular gas, Phys. Rev. E **97**, 032902 (2018).

[44] C. Zhang, W. R. Heinson, P. Liu, P. Beeler, Q. Li, J. Jiang, and R. K. Chakrabarty, Three-dimensional tomography reveals distinct morphological and optical properties of soot aggregates from coal-fired residential stoves in china, J. Quant. Spectrosc. Radiat. Transfer **254**, 107184 (2020).

[45] S. E. Leggett, Z. J. Neronha, D. Bhaskar, J. Y. Sim, T. M. Perdikari, and I. Y. Wong, Motility-limited aggregation of mammary epithelial cells into fractal-like clusters, Proc. Natl. Acad. Sci. USA **116**, 17298 (2019).

[46] C.-Y. Liu, H.-Y. Chen, and L. I., Scale-free aggregation and interface fluctuations of cancer clusters in cancer-endothelial cell mixtures: From the dilute state to confluent monolayer, Phys. Rev. Res. **3**, L032050 (2021).

[47] M. Simmler, M. Meier, and H. Nirschl, Characterization of fractal structures by spray flame synthesis using x-ray scattering, Materials **15**, 2124 (2022).

[48] S. Ostojic, D. Panja, and B. Nienhuis, Clustering in a one-dimensional inelastic lattice gas, Phys. Rev. E **69**, 041301 (2004).

[49] P. Meakin, Formation of fractal clusters and networks by irreversible diffusion-limited aggregation, Phys. Rev. Lett. **51**, 1119 (1983).

[50] J. Hoshen and R. Kopelman, Percolation and cluster distribution. I. Cluster multiple labeling technique and critical concentration algorithm, Phys. Rev. B **14**, 3438 (1976).

[51] K. Falconer, *Fractal Geometry: Mathematical Foundations and Applications* (John Wiley & Sons, Hoboken, 2004).

[52] T. A. Witten and L. M. Sander, Diffusion-limited aggregation, a kinetic critical phenomenon, Phys. Rev. Lett. **47**, 1400 (1981).

[53] J. M. Tenti, S. N. Hernández Guiance, and I. M. Irurzun, Fractal dimension of diffusion-limited aggregation clusters grown on spherical surfaces, Phys. Rev. E **103**, 012138 (2021).

[54] M. Kolb, R. Botet, and R. Jullien, Scaling of kinetically growing clusters, Phys. Rev. Lett. **51**, 1123 (1983).

[55] J. Wang, B. H.-j. Lee, and G. Arya, Kinetically assembled binary nanoparticle networks, Nanoscale **12**, 5091 (2020).

[56] S. Krishnamurthy, R. Rajesh, and O. Zaboronski, Kang-Redner small-mass anomaly in cluster-cluster aggregation, Phys. Rev. E **66**, 066118 (2002).

[57] S. Krishnamurthy, R. Rajesh, and O. Zaboronski, Persistence properties of a system of coagulating and annihilating random walkers, Phys. Rev. E **68**, 046103 (2003).

[58] R. Rajesh and O. Zaboronski, Survival probability of a diffusing test particle in a system of coagulating and annihilating random walkers, Phys. Rev. E **70**, 036111 (2004).